Accelerated Iterative Method for Solving Steady Problems of Linearized Atmospheric Models

Masahiro Watanabe[1]

Fei-fei Jin[2]

Lin-lin Pan[3]

1: Faculty of Environmental Earth Science, Hokkaido University

2: Department of Meteorology, Florida State University

3: International Pacific Research Center, University of Hawaii

Submitted to JAS, September 7, 2005

Revised, February 3, 2006

Revised, April 1, 2006

Corresponding authors:

M. Watanabe, Faculty of Environmental Earth Science, Hokkaido University

Nishi 5 Kita 10, Sapporo, Hokkaido 060-0810, Japan (E-mail: hiro@ees.hokudai.ac.jp)

F.-F. Jin, Department of Meteorology, Florida State University

Love Bldg, Tallahassee, FL32306-4520, USA (E-mail: jff@met.fsu.edu)

ABSTRACT

A new approach, referred to as the accelerated iterative method (AIM), is developed for obtaining steady atmospheric responses with zonally varying basic state. The linear dynamical operator is divided into two parts, one associated with the zonally symmetric component and the other with the asymmetric component of the basic state. To ensure an accelerated convergence of the iteration to the true solution, the two parts of the operator are modified by adding and subtracting an identical "accelerating" operator. AIM is shown to be an efficient scheme well suited for computing higher resolution, steady atmospheric response of barotropic and more so of baroclinic numerical models linearized about a zonally varying basic state.

A preliminary application of AIM to the T42 baroclinic model linearized about the observed winter (December-February) climatology is presented. A series of steady responses forced by the diabatic heating and transient eddy forcing, both estimated from reanalysis data for individual winters during 1960-2002, captures a certain part of the observed interannual variability associated with dominant teleconnection patterns, such as the North Atlantic Oscillation and the Pacific/North American pattern.

Thus AIM should be a useful tool for the diagnostic studies of the low-frequency variability of the atmosphere.

1. Introduction

Monthly and/or seasonal mean anomalies in the large-scale atmospheric circulation are central pieces for our understanding of the interannual climate variability. Regardless of their origin, whether forced by external forcing or generated through internal processes of the atmosphere, the spatial structures prevailing in such time-mean atmospheric anomalies have been classified into several teleconnection patterns (Wallace and Gutzler 1981; Barnston and Livezey 1987; Kushnir and Wallace 1989; among others). Understanding the generation and maintenance mechanisms of these teleconnection patterns is still an ongoing research topic (Wallace 2000; Hurrell et al. 2003; references therein).

In numerous studies, linearized atmospheric models are shown to be useful tools to elucidate dynamical processes of the time-mean atmospheric anomalies. In particular, the linear baroclinic model (LBM) that consists of primitive equations linearized about the climatological mean state has been developed by several research groups to reproduce the anomalies in the global atmosphere. This approach leaves out important questions regarding the dynamics for the observed climatological state. Nevertheless, the LBMs capture enough of the observed teleconnection patterns. In the classic paper of Hoskins and Karoly (1981), steady solutions forced by idealized thermal and orographic forcing are calculated based on the 5-level LBM. This study provides insights into the energy propagation of stationary Rossby waves and their association with the extratropical circulation anomalies observed during El Niño, which strongly project onto the so-called Pacific/North American (PNA) pattern (e.g., Horel and

Wallace 1981).

When the primitive equations are linearized about a zonally *uniform* state, as in Hoskins and Karoly (1981), the forced steady problem can be separately solved for each zonal wavenumber. Because of this simplification, models with this feature are important diagnostic tools called stationary wave model (SWM). These models are widely used to simulate either anomalous or climatological stationary waves (for a comprehensive review see Held et al. (2002)).

By examining steady solutions with a zonally *varying* basic state, it gradually became clear that the climatological zonal asymmetry in the basic state is crucially important for simulating the anomalous atmospheric circulation (Branstator 1990; Ting and Lau 1993; Ting and Sardeshmukh 1993; DeWeaver and Nigam 2000; Peng and Robinson 2001). Branstator (1990) demonstrated that the steady responses have a preferred structure with the 3D basic state even if the forcing is spatially random. Some of the prevailing patterns found in his LBM are quite similar to the patterns of dominant circulation anomalies identified in a general circulation model (GCM) about which the LBM is linearized, indicating that the coupling between the atmospheric anomalies and the climatological zonal asymmetry is one of the major sources for the large-scale, low-frequency variability of the extratropical atmosphere. Watanabe and Jin (2004) carried out a similar, but more sophisticated, analysis of the singular vectors of the LBM using the observed winter 3D climatology as the basic state. They showed that some of the dominant teleconnections may be regarded as near-neutral dynamical modes of the zonally asymmetric mean state.

When using the LBM with non-zonal basic states, we face a technical and critical obstacle: the linear dynamical operator matrix becomes too huge to be inverted

directly. In most of the previous studies in which steady responses are obtained by the matrix inversion technique one resorts to a coarse spatial resolution of, say, 15-20 zonal wavenumbers and less than 10 vertical levels (Navarra 1990; Branstator 1990; Ting and Held 1990; Ting and Lau 1993; Watanabe and Kimoto 2000). This reduction in spatial dimensions is often justified by arguing that the observed seasonal mean anomalies are dominated by planetary-scale components which are resolved adequately. However, the forcings in many cases have a much finer structure, and the small-scale eddies may modify large-scale eddies via their coupling with the zonal asymmetries in the basic state. The above then mitigates in favor of having much finer resolution.

There are at least two different ways to deal with the above dimensional constraint. The first method consists of simply integrating the model in time (Hall and Sardeshmukh 1998; Peng and Whitaker 1999; Peng and Robinson 2001). The time integration approach has the advantage that it can also handle nonlinear models (Jin and Hoskins 1995; Ting and Yu 1998). Its drawback is that it may not be very efficient computationally. The second method consists of solving the linear operator matrix with the help of advanced algorithms. For example, in Branstator (1992) steady responses are obtained using the out-of-core algorithm which saves the computer memory. Alternatively, DeWeaver and Nigam (2000) parallelized the model, rendering it very efficient in inverting large matrices by using scalable routines.

In the present study, an alternative method based upon a relaxation scheme is explored. Because the SWM* is much easier to solve than the full LBM, we construct a scheme that first calculates the steady response to a zonally symmetric basic state by the

* The SWM ordinarily refers to a model that solves only for wave components, but in this study the zonal-mean (wavenumber zero) component is also calculated.

direct method. We then correct that solution iteratively so as to satisfy a dynamical balance with the zonally varying basic state. We refer to this scheme as the accelerated iterative method or AIM; the "acceleration" is achieved through a modification of the linear operator that provides for, as we shall soon see, fast convergence of the numerical iteration.

This paper is organized as follows. The mathematical bases of AIM used in linearized atmospheric models are described in the next section. In section 3, the attributes of AIM, such as convergence, accuracy and comparison with other numerical methods, are examined for the case of the barotropic model. In section 4 AIM is applied to the LBM and emphasis is placed on hindcasting the observed interannual variability in the teleconnection patterns. A summary and discussion of this work are presented in section 5.

2. Models and methodology

a. Principle of AIM

The general expression describing the time evolution of linear atmospheric perturbations is written in the matrix form as

$$\frac{\mathrm{d}}{\mathrm{d}t}\mathbf{X}_a + \mathbf{L}(\mathbf{X}_c)\mathbf{X}_a = \mathbf{F} \quad , \tag{1}$$

where $\mathbf{X}_a$ denotes the perturbation state vector of the atmosphere, $\mathbf{F}$ is the external forcing, and $\mathbf{L}$ is the dynamical operator of the governing equations which is a linear function of basic state $\mathbf{X}_c$. For steady problems, a given forcing $\mathbf{F}$ is prescribed and the perturbation vector $\mathbf{X}_a$ is obtained by inverting $\mathbf{L}$ so that $\mathbf{X}_a = \mathbf{L}^{-1}\mathbf{F}$. This inversion is easily obtained for a small matrix, such as the one found in a barotropic model. As

mentioned in the introduction, LBMs, even those having coarse horizontal and vertical resolutions consisting of T21 in the horizontal and 20 levels in the vertical, the size of $\mathbf{L}$ exceeds 3×10^4. To proceed with the development of AIM, we divide the basic state into the zonally *symmetric* and *asymmetric* parts, denoted as $\bar{\mathbf{X}}_c$ and $\mathbf{X}_c^*$, respectively, and write (1) for a steady problem as

$$\mathbf{L}_S(\bar{\mathbf{X}}_c)\mathbf{X}_a + \mathbf{L}_A(\mathbf{X}_c^*)\mathbf{X}_a = \mathbf{F} \quad , \tag{2}$$

where $\mathbf{L}_S$ ($\mathbf{L}_A$) is the dynamical operator linearized about $\bar{\mathbf{X}}_c$ ($\mathbf{X}_c^*$). Since $\mathbf{L}_S$ consists of block matrices for each zonal wavenumber, it can be easily inverted. As a consequence an iterative scheme for (2) may be constructed as

$$\mathbf{X}_a^{\mathrm{n}+1} = -\mathbf{L}_S^{-1}\mathbf{L}_A\mathbf{X}_a^{\mathrm{n}} + \mathbf{L}_S^{-1}\mathbf{F} = \mathbf{M}\mathbf{X}_a^{\mathrm{n}} + \mathbf{G} \quad , \tag{3}$$

where n indicates the iteration step while the matrix $\mathbf{M}$ and the vector $\mathbf{G}$ represent the iteration operator and the modified forcing in the iterative scheme, respectively.

Equation (3) has the same form as the conventional Jacobian relaxation, leading to the convergence condition in terms of the spectral radius of $\mathbf{M}$ (cf. Meurant 1999; Kalnay 2003), namely

$$\rho(\mathbf{M}) = \max\left|\sigma_j\right| < 1 \quad , \tag{4}$$

where the spectral radius ρ is defined by the maximum of the absolute eigenvalues of $\mathbf{M}$, $\left|\sigma_j\right|$. As will be shown later, the condition (4) is in general not satisfied for the steady atmospheric problem.

We shrink the eigen-spectrum of $\mathbf{M}$ by introducing in (2) an accelerating operator matrix denoted as $\mathbf{R}$ so that

$$(\mathbf{L}_S + \mathbf{R})\mathbf{X}_a + (\mathbf{L}_A - \mathbf{R})\mathbf{X}_a = \mathbf{F} \quad . \tag{5}$$

The modified iterative scheme becomes

$$\mathbf{X}_a^{n+1} = (\mathbf{R}+\mathbf{L}_S)^{-1}(\mathbf{R}-\mathbf{L}_A)\mathbf{X}_a^{n} + (\mathbf{R}+\mathbf{L}_S)^{-1}\mathbf{F} \quad , \tag{6}$$

with $\mathbf{X}_a^0 = 0$. The acceleration matrix $\mathbf{R}$ in (6) is chosen to ensure that

$$\rho(\mathbf{M}^*) < 1 \quad , \tag{7}$$

where the iteration matrix $\mathbf{M}^*$ is defined as

$$\mathbf{M}^* \equiv (\mathbf{R}+\mathbf{L}_S)^{-1}(\mathbf{R}-\mathbf{L}_A) \quad , \tag{8}$$

The choice of the form of $\mathbf{R}$ in (8) is crucial for the success of AIM. The first criterion is that real parts of the eigenvalues of $\mathbf{R}$ are all positive, which is demonstrated as follows. When the norm of $\mathbf{R}$ is sufficiently large, we will have the following first order Taylor expansion to $\mathbf{M}^*$:

$$\mathbf{M}^* \approx \mathbf{I} - \mathbf{R}^{-1}\mathbf{L} \quad , \tag{9}$$

where $\mathbf{I}$ denotes an identity matrix and $\mathbf{L}$ is defined in (1). Since, by definition, all the eigenvalues of $\mathbf{R}$ have positive real parts, from (9), it turns out that the spectral radius $\rho(\mathbf{M}^*)$ is always smaller than 1 if the real parts of eigenvalues of $\mathbf{L}$ are all positive, i.e., no instability occurs. Thus when the operator $\mathbf{L}$ is dynamically stable or near neutral, the scheme (6) is guaranteed to converge.

Consider a simple case where $\mathbf{R} = \mathbf{I}/\Delta t$, Δt being the time interval used in the integration (1). This $\mathbf{R}$ satisfies the above criterion and (6) may be regarded as a semi-implicit scheme. Intuitively, in order to "accelerate" the "time stepping", larger (smaller) Δt may be used for large-scale (small-scale) waves. From this point of view, it would seem obvious that the choice of a scale dependent $\mathbf{R}$ would accelerate the scheme outlined in (6) and will yield in a steady solution in which different timescales

are used for different wave components in the spectral domain.

Furthermore, for computational efficiency, $\mathbf{R}$ ought to be decomposed into block matrices so that $\mathbf{R}+\mathbf{L}_S$ is inverted separately for each zonal wavenumber. For these reasons, we write $\mathbf{R}$ as:

$$\mathbf{R} = \gamma \mathbf{D} \quad , \tag{10}$$

where γ is a parameter while $\mathbf{D}$ is the matrix containing a scale-selective diffusion used in the model. The operator $\mathbf{D}$ becomes a diagonal matrix when this method is applied to spectral models. From the above choice of $\mathbf{R}$ in (10), it can be inferred that there is an optimal value of γ for fast convergence. When γ is zero, (6) reduces to (3) which may diverge. When γ is too large, the spectral radius of $\mathbf{M}^*$ will be close to 1, resulting in very slow convergence. It will be shown in the next section that indeed there is a certain moderate value of γ that makes the scheme (6) converge most rapidly. We note that when implementing the scheme (6), we only need to calculate and invert the block matrix ($\mathbf{R}+\mathbf{L}_S$) for each zonal wavenumber, which is done once and for all. There is no need to obtain and store the large matrix $\mathbf{L}_A$, rather we use the rhs terms of the model equations to directly calculate the vector $(\mathbf{R}-\mathbf{L}_A)\mathbf{X}_a^{\mathrm{n}}+\mathbf{F}$ as in the conventional tendency calculation for the time integration. Thus, each iteration requires nearly the same amount of calculations as if we were integrating the model one step forward. As long as the block matrices are inverted beforehand, the iteration does not involve any large matrix operations and thus AIM as expressed in (6) and (10) is highly efficient.

b. Linear atmospheric models

To verify the implementation of AIM, we use two different atmospheric models: a simplified one, which is easy to handle, and a complicated one which is more realistic, but computationally expensive. The former follows a barotropic vorticity equation linearized about the observed 300 hPa mean flow whereas the latter is the LBM which we have developed previously (Watanabe and Kimoto 2000, 2001; Watanabe and Jin 2004). Both models are based on the exact linearization of nonlinear spectral equations.

The barotropic model is used to examine the attributes of AIM, for example its convergence, efficiency, and resolution dependence; this investigation is presented in the next section in which the steady streamfunction response to an idealized tropical forcing is repeatedly calculated with different resolutions of T21, T42, T63, and T106. The model employs the biharmonic diffusion corresponding to **D** in (10), whose coefficients depend on the resolution used (see Table 1), and the Rayleigh friction with the damping timescale of 10 days. The model basic state is derived from the winter (December-February) mean climatology of the ECMWF reanalysis data (ERA40) during 1961-1990 (Uppala et al. 2006) while the idealized vorticity source which mimics the anomalous divergent forcing during El Niño follows Branstator (1985). We note that the characteristics of AIM crucially depend on the dynamical operator but not on the forcing structure.

We also have performed a series of the barotropic model calculations using the winter climatology derived from the NCEP-NCAR reanalysis data during 1949-1999 (Kalnay et al. 1996). The results are not shown, but are similar to those with the ERA40 basic state, except that the convergence is slightly different, mostly due to small difference in the $\mathbf{L}_A$ operator.

The LBM is based on an exactly linearized set of equations for vorticity (ς), divergence (*D*), temperature (*T*), and the logarithm of surface pressure ($\pi = \ln Ps$). The model variables are expressed horizontally by the spherical harmonics as in the barotropic model but the truncation is fixed at T42 while the finite difference is used for the vertical discretization which is fixed at 20 σ-levels. The model includes three dissipation terms: a biharmonic horizontal diffusion associated with ς, *D*, and *T*, a harmonic vertical diffusion (damping timescale of 1000 days) to remove a vertical noise arising from finite difference, and the Newtonian damping and Rayleigh friction as represented by a linear drag. The drag coefficients have a damping timescale of 0.5 days at the lowest four levels ($\sigma \geq 0.9$), and also at the topmost level to prevent a false wave reflection at the top boundary. In between these levels the $(30 \text{ days})^{-1}$ damping is applied, which does not seriously affect the amplitude and structure of the response. The boundary layer damping adopted here roughly follows the mixing coefficients evaluated with the Mellor-Yamada closure in the CCSR/NIES AGCM which we used to develop the LBM. These mixing coefficients are strong enough to neutralize baroclinic instability waves in the system (Hall and Sardeshmukh 1998). When applying AIM to this model, the coefficient of horizontal diffusion is an important parameter, which is fixed at a relatively large value corresponding to the damping timescale of 2 hours for the smallest wave. The basic state of the LBM is adopted from the winter 3D climatology of the ERA40 during 1961-1990, as in the barotropic model.

c. Forcings of the LBM

The forcings prescribed to LBM consist of anomalies of the diabatic heating and of the transient nonlinear terms also denoted as the transient eddy forcing; both forcings

are calculated using the 6-hourly ERA40 data during 1960-2002. The diabatic heating field is obtained as the residual of the thermodynamic equation in pressure coordinates (cf. Yanai et al. 1992). At the grids where the surface pressure is greater than 1000 hPa, the zero heating is interpolated when converting from the pressure to sigma coordinates. The winter anomalies of the diabatic heating are calculated by subtracting the monthly climatology for 1961-1990 from monthly fields, and taking the average during the winter season for 43 years. The transient nonlinear terms contain both the vorticity and thermal fluxes due to submonthly disturbances. Before calculating the eddy forcing, submonthly eddy fields are interpolated on to the T42 σ -surfaces, and then the horizontal and vertical fluxes of vorticity and sensible heat are calculated following the primitive equations used by the LBM. After the winter anomalies of these fluxes have been calculated, they are converted to the spectral space and the eddy forcings are calculated by taking the convergence of these fluxes. In the next two sections we focus on the attributes of AIM in the barotropic model, section 4, and in the LBM, section 5.

3. Verification of AIM using the barotropic model

a. Measures of convergence

In this section we investigate the efficient manner in which AIM reaches a steady forced solution in barotropic models. The approximate solution at each iteration step is compared to the true solution obtained beforehand by the conventional matrix inversion technique. The criterion for convergence, ε, is defined here by the RMS error between the true and AIM solutions,

$$\varepsilon^{\mathrm{n}} = \left\| \mathbf{X}_a - \mathbf{X}_a^{\mathrm{n}} \right\| / \left\| \mathbf{X}_a - \mathbf{X}_a^{1} \right\| \quad , \tag{11}$$

where $\mathbf{X}_a$ denotes the true solution represented by the anomalous streamfunction in case of the barotropic model, whereas $\mathbf{X}_a^{\mathrm{n}}$ is the AIM solution at nth step. In order to eliminate the dependence of ε on the model resolution and magnitude of the forcing, the RMS error is normalized by the error at the first step $\mathbf{X}_a^1$. For huge matrices which cannot be solved directly, as in case of the LBM, another measure of convergence is used; it does not involve the knowledge of the true solution and that measure is provided by the normalized differential norm,

$$\lambda^{\mathrm{n}} = \left\| \mathbf{X}_a^{\mathrm{n}} - \mathbf{X}_a^{\mathrm{n-1}} \right\| / \left\| \mathbf{X}_a^2 - \mathbf{X}_a^1 \right\| \quad (\mathrm{n}>1) \quad . \tag{12}$$

b. Basic properties of AIM

Figure 1 shows the RMS error ratio, ε, defined by (11) for the T21 barotropic model response; in that figure the evolution of ε is plotted for different values of γ (from 1 to 9). For $\gamma = 0$, corresponding to $\mathbf{M}^* = \mathbf{M}$, the error immediately increases exponentially. For $\gamma \le 5$, ε initially decreases and then increases as the number of iterations increase culminating to an AIM solution that blows up. When γ is 7, the error continuously decreases and reaches 10^{-3} around n=100. A similar evolution is found for $\gamma > 7$ with slightly slower convergence; therefore, AIM solutions for $\gamma \ge 7$ converge, those having with $\gamma = 7$ are the fastest to converge and that value is the best choice in this case. From Fig. 1 we note that the error reduction is not monotonic due to a small amplitude oscillation. This fluctuation disappears when **R** includes the linear drag as well, which, however, results in the slower convergence (not shown).

Section 2a showed that the spectral radius of $\mathbf{M}^*$ is reduced when γ is large,

ensuring convergence of AIM solutions for sufficiently large γ. Figure 2 provides a graphical verification of this. Plots of the eigenvalues in the complex domain clearly indicate for which value of γ the spectral radius $\rho(\mathbf{M})$ is greater than unity (Fig. 2a, b), implying divergence of AIM solutions, and for which values of γ the spectral radius is less than unity (Fig. 2c, d), implying convergence of AIM solutions. Since $\mathbf{M}^*$ approaches the identity matrix for $\gamma \to \infty$ (cf. (8)), it is not surprising that for $\gamma = 100$ the eigenvalues are clustered around (0, 1) in the complex plane (Fig. 2d). For the T21 barotropic model shown in Fig. 2, the best choice of γ is $\gamma = 7$ (cf. Fig. 1), in this case the eigen-spectrum is 'shrank' the most toward the origin (not shown).

It was shown in Fig. 1 that if we allow the 10% (1%) error, only 12 (40) steps are necessary to obtain the steady response for the T21 model (see also Table 1). Efficiency of this convergence rate is compared with that in the other two iterative methods: the conventional time integration and the conjugate gradient (CG) method, the latter also known in the Krylov subspace techniques (Greenbaum 1997). The time integration employs the interval of Δt=60 minutes which is determined from the CFL condition. The CG method is applied on a symmetric matrix, so that the transpose of $\mathbf{L}$ has been multiplied to $\mathbf{L}$ before the iteration. To justify the comparison, both time integration and CG solver adopt the first guess $\mathbf{X}_a^1$ obtained from AIM. The result in terms of the RMS error ratio is presented in Fig. 3, which shows that AIM is the most efficient scheme. The iteration steps for the steady solution with 10% error are 12 for AIM, 147 for CG, and 379 for the time integration (roughly 16 days), respectively.

The spatial pattern of the streamfunction response to the idealized vorticity forcing is displayed in Fig. 4a. While the structure of the response is not the subject in

the present test, one clearly sees the stationary Rossby waves emanating from the equator into both hemispheres, a feature found in many studies (e.g., Branstator 1985). A first guess for the AIM solution with $\gamma = 7$ is shown in Fig. 4b; it also reveals such wave trains even though their amplitude is weaker than the true solution. The steady solutions in CG and AIM with the 1% RMS error obtained at n=292 and n=40, respectively, are almost identical to the true response (Figs. 4c and 4d). The overall pattern and amplitude of these approximate solutions are quite similar even when the error is 10% (not shown).

c. Dependence on the intrinsic diffusion

In choosing the form of $\mathbf{R}$, we have considered that the scale-selective matrix acts as accelerator of the iteration and that the efficiency is controlled by γ. We note that the inertia of each wave depends on the magnitude of the intrinsic diffusion of the system, i.e., $\mathbf{D}$ in (10); therefore, the convergence efficiency of AIM may also be affected by changing $\mathbf{D}$. Specifically, it is reasonable to speculate that the convergence of the AIM solution will be slower (faster) for weaker (stronger) intrinsic diffusion of the dynamical operator. The is verified by evaluating ε in the T21 barotropic model used in Fig. 1 but with the e-folding decay timescale of the horizontal diffusion altered from 1 day to either half a day or 2 days. In both cases the AIM solution successfully converged with the best choice of γ, which varies from the original value. The resultant profiles of ε reveal that the iteration steps drastically change when smaller values of ε are used to measure the convergence (Fig. 5). For $\varepsilon = 0.01$ (1% error), which is a typical threshold, the necessary iteration is shortened to 24 steps with stronger diffusion

while lengthened to 82 steps with weaker diffusion.

The result shown in Fig. 5 indicates that the convergence rate is highly sensitive to the magnitude of diffusion present in the dynamical operator. This result may also imply that the computational efficiency of AIM remains the same for different spatial resolutions as long as the diffusion coefficient is preserved. This is indeed seen in Fig. 6 which summarizes the iteration steps for convergence at various resolutions. In that figure, for $\varepsilon = 0.01$, AIM's last step, n, is calculated in barotropic models at T21, T42, T63, and T106. Three methods of iteration were used and the results of each of these methods are presented. The number of the degrees of freedom (gray line) provides the theoretical maximum of n for CG and AIM. When the diffusion coefficient is kept fixed at the T21 version, the iteration steps for CG and time integration increase at higher resolution while those for AIM are almost constant (dashed lines in Fig. 6). This comparison clearly demonstrates that AIM is the most efficient method, in particular with higher resolution. While this resolution-independent property is one of the advantages of AIM, this advantage may not be implemented in practice since the diffusion is resolution dependent. To wit, the decay time of 24 hours in T21 corresponds to 1.5 hours in T42, 19 minutes in T63, and only 2.4 minutes in T106. In general, the scale-selective diffusion is included to remove the enstrophy accumulation near the truncated wavenumber, so that a strong diffusion does not make physical sense. When we used more 'plausible' diffusion coefficients which are smaller at higher resolution (see Table 1), the convergence rate of AIM, as well as that of the other two methods, depends on the resolution (solid lines in Fig. 6). Nevertheless, AIM is still shown to be much more efficient than CG, and more than one order faster than the time integration.

Before extending AIM to the LBM, the relationship between the RMS error ratio

(ε) and the differential norm (λ) is briefly examined in the barotropic framework. Figure 7 shows the evolution of λ against ε of the AIM solutions at different resolutions. The solutions used here correspond to the solid line in Fig. 6 (i.e., the diffusion coefficients are not common among four resolutions), but the result is essentially the same for solutions with the common diffusion coefficients. Overall, the two measures shown in Fig. 7 are linearly proportional, inferring that $\lambda \approx 0.01$ roughly corresponds to the 1-3% error in ε[*].

4. Application to LBM

a. Simulation of 1997/98 anomalies

In the previous section, AIM was found to be a very efficient scheme when used in a barotropic model; in this section AIM is applied to the more challenging LBM. As described in section 2b, the ERA40 winter climatology during 1961-1990 was used as the basic state. Following Fig. 7, the convergence is evaluated with the threshold of $\lambda = 0.01$. As an example of the LBM diagnosis, 1997/98 winter anomaly field is chosen since it exhibits a large ENSO teleconnection. Figure 8a shows the horizontal wind anomalies at 850 hPa and the geopotential height anomaly at 300 hPa as observed during winter 1997/98, and illustrating the PNA-like circulation anomaly over the North Pacific in addition to the anomalous westerly (easterly) over the equatorial Pacific (Indian) Ocean. On one hand, when AIM is used with the T42 20-level LBM with the zonally *asymmetric* basic state to calculate the steady linear response to the combined forcing of diabatic heating and transient eddy fluxes, cyclonic and anticyclonic

[*] The reduction of λ tends to be slow for $\lambda < 0.01$, so that the threshold of $\lambda = 0.01$ greatly saves the computational time while the solution is quite similar to that with one order smaller λ.

anomalies appear at the correct positions over the North Pacific and North America, respectively (Fig. 8b). On the other hand, when the steady LBM response with the zonally *symmetric* basic state, i.e., SWM, is used the solution reveals that the equatorial wind anomaly is reproduced but the PNA-like pattern is not well reproduced (Fig. 8c). The difference between Figs. 8b and 8c points at the significant role of climatological stationary eddies in forming the extratropical teleconnection patterns, as was outlined in the introduction. The LBM response pattern in Fig. 8b is overall quite similar to the observation while there are discrepancies as well: the circulation anomaly over northern Eurasia is shifted to the west and the response over the PNA region is slightly weaker than the observation.

The sea level pressure (SLP) response associated with Fig. 8b is compared to the observed SLP anomaly (Figs. 9a and 9b). Except for the polar cap away 80°N, the steady SLP response captures the major high and low pressure anomalies. It should be noted, however, that the magnitude of the SLP response is about 70% of the observed anomaly. The cause of this underestimation plausibly comes from the difference in the vertical profile of temperature anomalies. The vertical structure of the observed temperature anomaly at 50°N indicates that the maxima are occurring near the surface, in particular, over land regions (Fig. 9c). In LBM, such large temperature response is not found because of the strong boundary layer damping which is necessary to prevent the baroclinic instability (Fig. 9d). Following the hydrostatic relation, the geopotential height response becomes weak as well, resulting in underestimation of the SLP response which is related to the vertical integral of the height response. The uniform drag on σ surfaces does not affect the horizontal structure of the response, so that the SLP response which has a reasonable spatial pattern is considered to be a relevant quantity in

evaluating the reproducibility of LBM solutions.

b. LBM hindcast

Despite some discrepancies, LBM solutions capture many features of the observed atmospheric anomalies during 1997/98 El Niño. Encouraged by this result, we attempted to hindcast the anomaly fields for 1960-2002 by solving the steady problem for each winter. For comparison the steady response with the zonally symmetric basic state is also calculated; we will refer to solution as the "SWM hindcast".

The capability of LBM in hindcasting the winter anomaly fields is first evaluated with the standard deviation of the 500 hPa height anomalies (Fig. 10). In observations, the maxima of the height variance are identified over the central North Pacific, Greenland, and north of Siberia, respectively (Fig. 10a). The height standard deviation in the full LBM hindcast (Fig. 10b) is comparable to observations both in terms of the amplitude and the position of maxima. The variance distribution over the North Pacific is the exception, which reveals the center split into two parts, unlike Fig. 10a. The standard deviation of the SWM hindcast (Fig. 10c) shows a pattern similar to the observations but weaker in magnitude. However, the locations of all the maximum variances do not coincide with observations, except for the peak south of Greenland. Since the zonally symmetric response has a significant contribution to the variance map, the SWM hindcast in which the zonally symmetric component is less reliable produces a worse result.

A more challenging task of the LBM hindcast is to examine the extent to which the interannual variability of the dominant teleconnections can be simulated. The first attempt is simply to compare several climate indices: Southern Oscillation Index (SOI),

PNA index, and the North Atlantic Oscillation (NAO) index. The SOI is conventionally defined by the normalized SLP difference between Tahiti and Darwin, while the PNA and NAO indices are defined with four action centers on the 500 hPa height (Wallace and Gutzler 1981) and normalized SLP difference between Lisbon and Stykkisholmur (cf. Hurrell et al. 2003), respectively. Correlation coefficients between these indices obtained from observations and the LBM hindcast were 0.87 for SOI, 0.34 for PNA, and 0.39 for NAO. Since the tropical atmosphere is known to obey simpler linear dynamics than say the midlatitude, it is not surprising that the hindcast SOI has a remarkable similarity to the observed index. The interannual variations in PNA and NAO indices are more difficult to be reproduced, so that the correlation between the observed and hindcast time series is significant but not as high as we expected.

The above results suggest that LBM captures, though not completely, a certain part of the extratropical atmospheric variability. To investigate further, we compared patterns of the leading empirical orthogonal function (EOF) to the winter SLP anomalies between ERA40 and the LBM hindcast. The EOF analysis is applied to the North Pacific (150°E-90°W, 20°-90°N) and to the North Atlantic (50°W-40°E, 20°-90°N) separately in order to extract the regional features. The observed leading EOFs, which account for 40.6% and 48.3% of the total variance in each field, reveal the PNA and NAO, as presented by the 500 hPa height anomalies regressed on to the associated principal components (PCs) (Fig. 11a, b). The leading EOFs obtained from the LBM hindcast (Fig. 11c, d) do show similar patterns with slightly smaller fractional variance, even though the PNA-like structure is somewhat weak (Fig. 11c) and the NAO-like pattern accompanies another center over north of Siberia (Fig. 11d). Indeed, the PC time series for both the observed and hindcast EOFs (Fig. 12) are highly correlated with each

other (the correlation reaches 0.57 for the Pacific and 0.56 for the Atlantic), indicating that the LBM reproduces the interannual variability of the PNA and NAO to a certain degree. The correlation of the PC time series of the Pacific EOF with the observed PNA index is 0.73 for the ERA40 data while 0.55 for the LBM hindcast. A similar result is obtained with the observed NAO index: 0.78 for the reanalysis and 0.47 for the hindcast. In the hindcast, their spatial patterns contain some distortion (cf. Fig. 11c, d), which leads to worse reproduction of the station-based indices as described.

The EOF analysis is also performed to the SWM hindcast (Fig. 11e, f). As highlighted in our Fig. 8 and in literatures (e.g., Ting and Lau 1993), SWM lacks an important source for the midlatitude circulation variability, namely, an energy conversion mechanism from the zonal asymmetry in the climatological state to the anomalous eddies, so that the leading EOFs are not only less similar to the observed patterns of PNA and NAO, but also less coherent (the correlation of the PC times series with the observed counterparts is 0.38 for the Pacific and 0.33 for the Atlantic).

Once the dominant teleconnection is identified in the hindcast, the linearity enables us to attribute the prevalence to the individual forcing terms. To examine the relative role of the diabatic heating and transient eddy forcing to the leading EOF patterns shown in Figs. 11c and 11d, 500 hPa height responses forced by one of these forcings are regressed upon the PC time series. Shown in Figs. 13a and 13b are the regressed height responses forced only with the diabatic heating. While the magnitude is about one third of the total response, they apparently project well onto the EOF patterns. It is noted that the regressed height responses have similar patterns in the SWM hindcast as well (Figs. 13c and 13d), implying that the linear response to the diabatic heating is less sensitive to the zonal asymmetry in the basic state, as found in

Peng and Whitaker (1999). If we refer to the previous works that emphasized the role of the so-called zonal-eddy coupling in forming the dominant teleconnections (DeWeaver and Nigam 2000; Watanabe and Jin 2004), this result suggests that the thermally forced response is primarily explained by simple stationary wave dispersion, with weak coupling with the zonal-mean anomalies. The regressed height responses forced only by the transient eddies, dominated by the eddy vorticity forcing, reveal larger magnitude and also have a strong projection onto the leading EOF patterns (not shown). Whether the thermally induced response in Figs. 13a and 13b can modulate the Pacific and Atlantic storm tracks, respectively, so as to force the pattern in Figs. 11c and 11d, i.e., while providing a positive feedback between the anomalous stationary eddies and transients, is beyond the scope of this study. Previous works support such a possibility (Peng and Whitaker 1999; Watanabe and Kimoto 2000; Peng and Robinson 2001; Pan et al. 2006).

It is interesting to regress with the model's PC time series not only of the hindcast response but also of the forcing, which clarifies the optimal forcing structure. While the regressed pattern of the eddy forcing is quite noisy, the regression of the diabatic heating is more systematic (Fig. 14). For the PNA-like mode of variability shown in Figs. 11c and 13a, the heating has a deep vertical structure in the tropical Pacific, reminiscent of a typical precipitation anomaly pattern during El Niño (Figs. 14a and 14c). We note that the vertically averaged heating associated with the NAO-like variability shown in Figs. 11d and 13b has only a weak anomaly in the central equatorial Pacific (Fig. 14b), confirming that the NAO is less controlled by the remote tropical heating. However, it is noteworthy that a set of shallow heating and cooling anomalies is detected in the North Atlantic, which is likely to optimally force the NAO-

like variability (Fig. 14d). These anomalies are confined below $\sigma = 0.7$ (vertical structure not shown), suggesting that they are related to the anomalous sensible and latent heat fluxes due to changes in storm track and sea surface temperature (SST). The heating anomalies in the North Atlantic thus appear to be partly indicative of the so-called tripole SST forcing the NAO (Rodwell et al. 1999; Graham et al. 2005; among others).

5. Summary and discussion

In the past decade, on one hand numerical studies on the climate variability have used higher resolution GCMs. On the other hand, linearized atmospheric models have been shown to be relevant in delineating dynamical processes of the atmospheric anomalies. These models have been used at a coarse resolution due to practical constraint of inverting large matrices associated with the linear dynamical operator used in solving steady forced problems with the zonally asymmetric basic state. Motivated by the desire to solve these steady problems and dealing with LBM having a satisfactory resolution, we proposed an efficient method, called AIM, based on a relaxation algorithm.

The central idea of AIM is to decompose the linear operator matrix into a group of block matrices associated with the zonally uniform part of the basic state and a large matrix associated with the non-zonal part; the block matrices can be easily inverted then the solution with the zonally uniform basic state is iteratively corrected by manipulating the latter. In general, such iteration does not converge for the dynamical equations of atmospheric models. An additional matrix ($\mathbf{R}$, see section 2a) is introduced, not only to ensure the convergence but also to accelerate the iteration. The asymptotic convergence

to the true solution is accomplished by choosing **R** adequately which involves selecting the single parameter γ judiciously.

The efficiency of AIM is first tested with the linear barotropic model (section 3). It is shown that AIM is successful in obtaining the steady solution with quite a small number of iterations. While the convergence rate is sensitive to the magnitude of intrinsic diffusion of the system, it is more than one order faster than the other iterative methods such as the time integration of the linear model. AIM is then applied to calculate the steady response with LBM in section 4. Given the thermal and momentum forcing due to diabatic processes and transient eddies estimated from the reanalysis data, LBM was shown to be capable of simulating the circulation anomalies during 1997/98 El Niño.

Steady solutions were then obtained in a similar manner for individual 43 winters during 1960-2002, composing the hindcast anomalies using the LBM. Despite several discrepancies, the LBM hindcast shows the variance distribution of the northern extratropical height anomalies to be comparable to the observations, and reproduces a certain fraction of the interannual variability associated with the dominant teleconnection patterns such as PNA and NAO; those indices based on the hindcast responses are significantly correlated with the observed indices. Taking advantage of linearity, the model PNA and NAO as identified by the leading EOFs to the hindcast SLP anomalies can be divided into the direct, thermally induced response and the response to anomalous transients. The former has a strong projection on to the principal patterns of variability, and is optimally forced by the deep heating in the equatorial Pacific for PNA while the NAO is forced by the shallow heating in the North Atlantic.

AIM includes procedures for preparing and inverting the linear dynamical

operator matrices for each zonal wavenumber with respect to the zonally asymmetric part of the basic state. The most efficient application of AIM would therefore be to compute a number of steady responses with the same basic state but different forcing, such as the hindcast presented in section 4b. While the algorithm of AIM appears to be already efficient in the practical applications, further acceleration may be possible by changing the definition of $\mathbf{R}$. We have examined the possibility, but currently have not obtained a form of $\mathbf{R}$ better than that found in (10); then, this issue remains a future research problem.

The LBM hindcast was able to simulate the dominant low-frequency variability to some extent, but its reproducibility in terms of spatial and temporal fluctuations is not satisfactory (Figs. 11 and 12). This failure probably arises from an inaccuracy of the forcing terms. Since ERA40 data are provided on a linear grid at each pressure level, the forcing fields have to be interpolated both horizontally and vertically, resulting in an increase in the error. In particular, shallow heating over regions where surface pressure is above 1000 hPa cannot be adequately estimated from the pressure level data. We note that LBM forced by the forcing obtained from a GCM that shares the dynamical framework has been shown to yield better results in reproducing the low-frequency variability in the GCM (e.g., Ting and Lau 1993). We are currently testing the LBM hindcast and using AIM with GCM-generated anomalies. These investigations will be reported elsewhere. As a caveat, we note that the boundary layer mixing is modeled by a uniform drag, yet in nature it varies in space and depends on the stability and shear of the basic state (cf. DeWeaver and Nigam 2000). Errors associated with this coarse physical modeling may be present in the results we reported above.

As in most of previous studies, steady atmospheric problems are solved in this

study by prescribing the forcing due to diabatic processes and transient eddies. They are, however, partly dependent on the anomalous atmosphere, so that the LBM diagnosis is not actually closed. Our ultimate goal is to construct a linear atmospheric model that includes interactive moist processes (Watanabe and Jin 2003) and a linear closure for the two-way feedback between transient eddies and low-frequency anomalies (Jin et al. 2006; Pan et al. 2006). These extensions may enable us to develop a coupled atmosphere-ocean model using LBM, in which a steady atmospheric component accommodates not only high resolutions but also other complexities much beyond Gill-type intermediate models. For this purpose, we believe that AIM becomes a necessary and useful method and a handy tool for solving the steady atmospheric type of problems discussed in this work.

Acknowledgments. The authors thank A. Barcilon and three anonymous reviewers for their constructive comments. MW is supported by a Grant-in-Aid for Scientific Research from MEXT, Japan, and FFJ is supported by NOAA grants GC01-229 and GC01-246, NSF grants ATM-0226141 and ATM-0424799. This work was initiated during MW's visit at the Department of Meteorology, Florida State University in March 2005, when MW obtained the mathematical scheme of AIM designed by FFJ.

REFERENCES

Barnston, A. G., and R. E. Livezey, 1987: Classification, seasonality and persistence of low-frequency atmospheric circulation patterns. *Mon. Wea. Rev.*, **115**, 1083-1126.

Branstator, G., 1985: Analysis of general circulation model sea-surface temperature anomaly simulations using a linear model. Part I: Forced solutions. *J. Atmos. Sci.*, **42**, 2225-2241.

Branstator, G., 1990: Low-frequency patterns induced by stationary waves. *J. Atmos. Sci.*, **47**, 629-648.

Branstator, G., 1992: The maintenance of low-frequency atmospheric anomalies. *J. Atmos. Sci.*, **49**, 1924-1945.

DeWeaver, E., and S. Nigam, 2000: Zonal-eddy dynamics of the North Atlantic Oscillation. *J. Climate*, **13**, 3893-3914.

Graham, R. J., and Co-authors, 2005: A performance comparison of coupled and uncoupled versions of the Met Office seasonal prediction general circulation model. *Tellus*, **57A**, 320-339.

Greenbaum, A., 1997: *Iterative methods for solving linear systems.* In "Frontiers in Applied Mathematics", SIAM, 220pp.

Hall, N. M. J., and P. D. Sardeshmukh, 1998: Is the time-mean Northern Hemisphere flow baroclinically unstable? *J. Atmos. Sci.*, **55**, 41-56.

Held, I. M., M. Ting, and H. Wang, 2002: Northern winter stationary waves: Theory and modeling. *J. Climate*, **15**, 2125-2144.

Held, I. M., S. W. Lyons, and S. Nigam, 1989: Transients and the extratropical response to El Niño. *J. Atmos. Sci.*, **46**, 163-174.

Horel, J. D., and J. M. Wallace, 1981: Planetary-scale atmospheric phenomena associated with the Southern Oscillation. *Mon. Wea. Rev.*, **109**, 813-829.

Hoskins, B. J., and D. J. Karoly, 1981: The steady linear responses of a spherical atmosphere to thermal and orographic forcing. *J. Atmos. Sci.*, **38**, 1179-1196.

Hurrell, J. W., Y. Kushnir, G. Ottersen, and M. Visbeck, 2003: An overview of the North Atlantic Oscillation. In "*The North Atlantic Oscillation*", Hurrell, J. W., Y. Kushnir, G. Ottersen, M. Visbeck eds., *Geophysical Monograph*, **134**, 1-35.

Jin, F.-F., L.-L. Pan, and M. Watanabe, 2006: Dynamics of synoptic eddy and low-frequency flow interaction. Part I: A linear closure. *J. Atmos. Sci.*, in press.

Jin, F.-F., and B. J. Hoskins, 1995: The direct response to tropical heating in a baroclinic atmosphere. *J. Atmos. Sci.*, **52**, 307-319.

Kalnay, E., and Co-authors, 1996: The NCEP/NCAR 40-year reanalysis project. *Bull. Amer. Meteor. Soc.*, **77**, 437-471.

Kalnay, E., 2003: *Atmospheric modeling, data assimilation and predictability*. Cambridge University Press, 341pp.

Kushnir, Y., and J. M. Wallace, 1989: Low-frequency variability in the Northern Hemisphere winter: Geographical distribution, structure and time-scale dependence. *J. Atmos. Sci.*, **46**, 3122-3142.

Meurant, G., 1999: *Computer solution of large linear systems*. Elsevier, 776pp.

Navarra, A., 1990: Steady linear response to thermal forcing of an anomaly model with an asymmetric climatology. *J. Atmos. Sci.*, **47**, 148-169.

Pan, L.-L, F.-F Jin, and M. Watanabe, 2006: Dynamics of synoptic eddy and low-frequency flow interaction. Part III: Baroclinic model results. *J. Atmos. Sci.*, in press.

Peng, S., and J. S. Whitaker, 1999: Mechanisms determining the atmospheric response to midlatitude SST anomalies. *J. Climate*, **12**, 1393-1408.

Peng, S., and W. A. Robinson, 2001: Relationships between atmospheric internal variability and the responses to an extratropical SST anomaly. *J. Climate*, **14**, 2943-2959.

Rodwell, M. J., D. P. Rowell, and C. K. Folland, 1999: Oceanic forcing of the wintertime

North Atlantic Oscillation and European climate. *Nature*, **398**, 320-323.

Ting, M., and I. M. Held, 1990: The stationary wave response to a tropical SST anomaly in an idealized GCM. *J. Atmos. Sci.*, **47**, 2546-2566.

Ting, M., and N.-C. Lau, 1993: A diagnostic and modeling study of the monthly mean wintertime anomalies appearing in a 100-year GCM experiment. *J. Atmos. Sci.*, **50**, 2845-2867.

Ting, M., and P. D. Sardeshmukh, 1993: Factors determining the extratropical response to equatorial diabatic heating anomalies. *J. Atmos. Sci.*, **50**, 907-918.

Ting, M., and L. Yu, 1998: Steady response to tropical heating in wavy linear and nonlinear baroclinic models. *J. Atmos. Sci.*, **55**, 3565-3582.

Uppala, S. M., and Co-authors, 2006: The ERA-40 re-analysis. *Quart. J. R. Met. Soc.*, in press.

Wallace, J. M., 2000: North Atlantic Oscillation/annular mode: Two paradigms-one phenomenon. *Quart. J. R. Met. Soc.*, **126**, 791-805.

Wallace, J. M., and D. S. Gutzler, 1981: Teleconnections in the geopotential height field during the Northern Hemisphere winter. *Mon. Wea. Rev.*, **109**, 784-812.

Watanabe, M., and M. Kimoto, 2000: Atmosphere-ocean thermal coupling in the North Atlantic: A positive feedback. *Quart. J. R. Met. Soc.*, **126**, 3343-3369; Corrigendum. *Quart. J. R. Met. Soc.*, **127**, 733-734.

Watanabe, M., and F.-F. Jin, 2003: A moist linear baroclinic model: Coupled dynamical-convective response to El Niño. *J. Climate*, **16**, 1121-1139.

Watanabe, M., and F.-F. Jin, 2004: Dynamical prototype of the Arctic Oscillation as revealed by a neutral singular vector. *J. Climate*, **17**, 2119-2138.

Yanai, M., C. Li, and Z. Song, 1992: Seasonal heating of the Tibetan Plateau and its effects on the evolution of the Asian summer monsoon. *J. Meteor. Soc. Japan*, **70**, 319-351.

FIGURE AND TABLE CAPTIONS

Fig.1 RMS error ratio (ε) of the AIM solution as a function of the iteration step n. All the errors are computed by the T21 barotropic model with different values of γ. The fastest convergence is obtained with $\gamma = 7$, as indicated by the thick curve .

Fig.2 Eigenvalue spectrum of $\mathbf{M}^*$ in the T21 barotropic model with (a) $\gamma = 0$ (equal to $\mathbf{M}$), (b) $\gamma = 1$, (c) $\gamma = 10$, and (d) $\gamma = 100$. σ_i and σ_r are the imaginary and real parts, respectively. A unit circle is drawn for reference.

Fig.3 Same as Fig.1 but for ε calculated from three different methods: AIM with $\gamma = 7$, time integration, and conjugate gradient method. The 10% and 1% error levels are indicated by dashed lines. Note that three methods employ the same first guess.

Fig.4 Steady streamfunction response to the equatorial divergent forcing (denoted by shading) obtained from the T21 barotropic model. The contour interval is 1×10^6 m^2 s^{-1} while the negative contours are dashed. (a) True solution by the matrix inversion, (b) the AIM solution at n=1 with $\gamma = 7$, (c) the CG solution at n=292, and (d) the AIM solution at n=40. The RMS errors for (c) and (d) are 1%.

Fig.5 Same as Fig.1 but for ε calculated with different diffusion coefficients, varying from 12hr to 2dy damping timescale for the smallest wave. The best value of γ employed in each computation is also indicated.

Fig.6 Number of iteration steps required for the convergence $\varepsilon \le 0.01$ in the barotropic model with different horizontal resolution. Dashed lines with circle, triangle, and cross show the solutions obtained from AIM, CG, and time integration, respectively,

all employing the diffusion coefficient common to the T21 resolution. Solid lines are the solutions with the diffusion dependent on the resolution (weaker in higher resolution, following Table 1). The gray line indicates the number of degrees of freedom.

Fig.7 Differential norm ratio, λ, against the companion RMS error ratio, ε, for the AIM solutions in the barotropic model. The values are plotted up to n=70 for T21, n=300 for T42, n=400 for T63, and n=800 for T106, respectively. The diffusion timescale for each resolution follows Table 1.

Fig.8 Anomalies of the 850 hPa wind (vector, plotted for the magnitude greater than 1 m s^{-1}) and 300 hPa geopotential height (contour, interval of 40 m without zero contours) (a) observed during winter 1997/98, and (b), (c) obtained as a steady response to the observationally estimated forcing. The responses are calculated with T42 20-level LBM, with the 3D basic state in (b) and the zonally uniform basic state in (c). The supplemental thin contour of 20 m is also indicated in (b) and (c).

Fig.9 (a) Observed and (b) calculated SLP anomalies during winter 1997/98, the latter associated with the steady response shown in Fig. 8b. The contour interval is 2 hPa, the zero contours omitted. (c), (d) Same as (a), (b) but for the temperature (contour, 1K interval) and height (shading) anomalies along 50°N. Topography resolved in LBM is presented by the black rectangles in (d).

Fig.10 Standard deviations of the 500 hPa height anomalies during 1960-2002, obtained from (a) ERA40, (b) the T42 LBM hindcast , and (c) the T42 SWM hindcast. The contour interval is 5m.

Fig.11 Leading EOFs to the winter SLP anomalies over the North Pacific (150°E-90°W, 20°-90°N) (left) and the North Atlantic (50°W-40°E, 20°-90°N) (right), as represented by the regression of the 500 hPa height anomalies on to the leading principal

components in each sector. (a), (b) ERA40, (c), (d) LBM hindcast, and (e), (f) SWM hindcast. The contour interval is 10 m, with the zero line denoted by thin contour. The fractional variance of the respective EOF1 is also indicated at the top-right of each panel.

Fig. 12 (a) The PC time series of the leading EOFs over the North Pacific shown in Fig. 11a, c. The solid (dashed) line indicates the observed (LBM hindcast) time series. (b) Same as (a) but for the leading EOFs over the North Atlantic shown in Fig. 11b, d. The correlation coefficients between the observed and hindcast time series are also shown at the top-right.

Fig.13 (a), (b) Same as Fig. 11c, d but for the regression of the hindcast response forced only by the diabatic heating anomalies. (c), (d) Same as (a), (b) but for the hindcast with zonally uniform basic state. The contour interval is 3 m.

Fig.14 (a), (b) Same as Fig. 11c, d but for the regression of the vertically averaged heating. (c), (d) Same as (a), (b) but for the heating averaged in the lower troposphere ($\sigma \geq 0.8$). The contour interval is 0.2 K day^{-1}. The zero contours have been omitted and negative contours dashed.

Table 1 Parameters used in the barotropic model with different horizontal resolution. The definitions of the RMS error ε and norm ratio λ are respectively given in Eqs. (11) and (12).

Table 1 Parameters used in the barotropic model with different horizontal resolution. The definitions of the RMS error ε and norm ratio λ are respectively given in Eqs. (11) and (12).

	T21	T42	T63	T106
Diffusion				
Order	4th	4th	4th	4th
Coefficient (10^{16} m^4/s)	8.93	1.75	0.47	0.18
Damping time (hour)	24	8	6	2
Best value of γ	7	40	127	350
Δt for time integration (min)	60	30	20	12
n for ε=0.1	12	54	129	329
n for ε=0.01	40	138	275	660
λ for ε=0.1	0.067	0.062	0.031	0.032
λ for ε=0.01	0.009	0.009	0.005	0.003
Degrees of freedom	483	1848	4095	11448

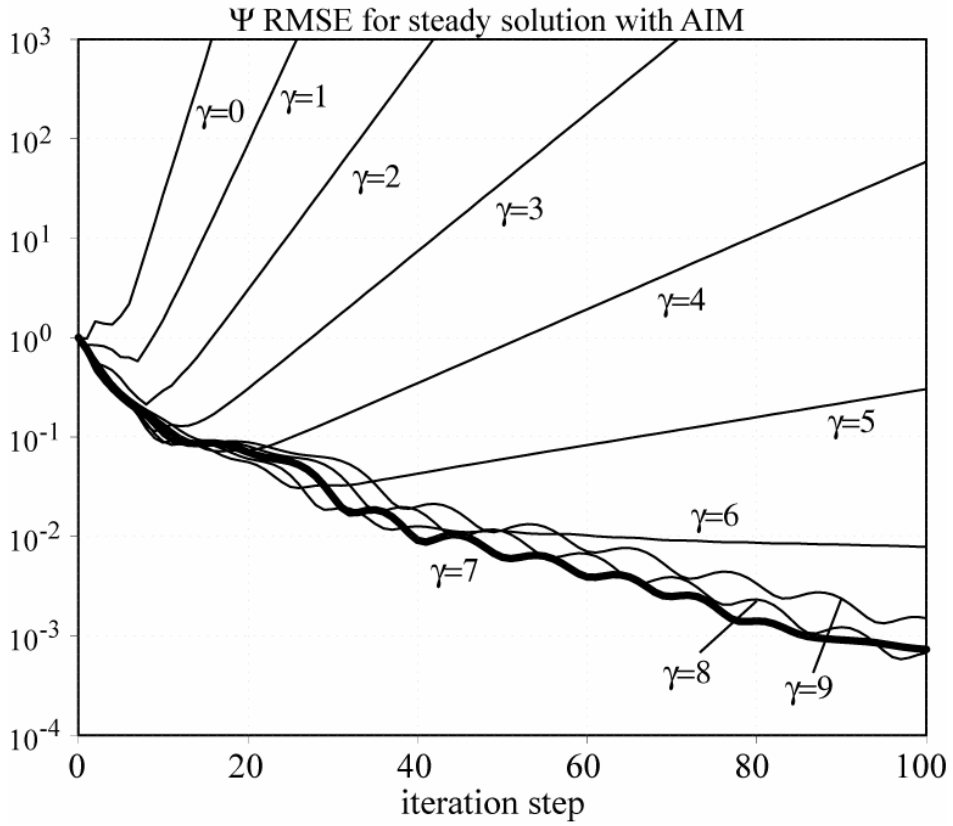

Fig.1 RMS error ratio (ε) of the AIM solution as a function of the iteration step n. All the errors are computed by the T21 barotropic model with different values of γ. The fastest convergence is obtained with $\gamma = 7$, as indicated by the thick curve .

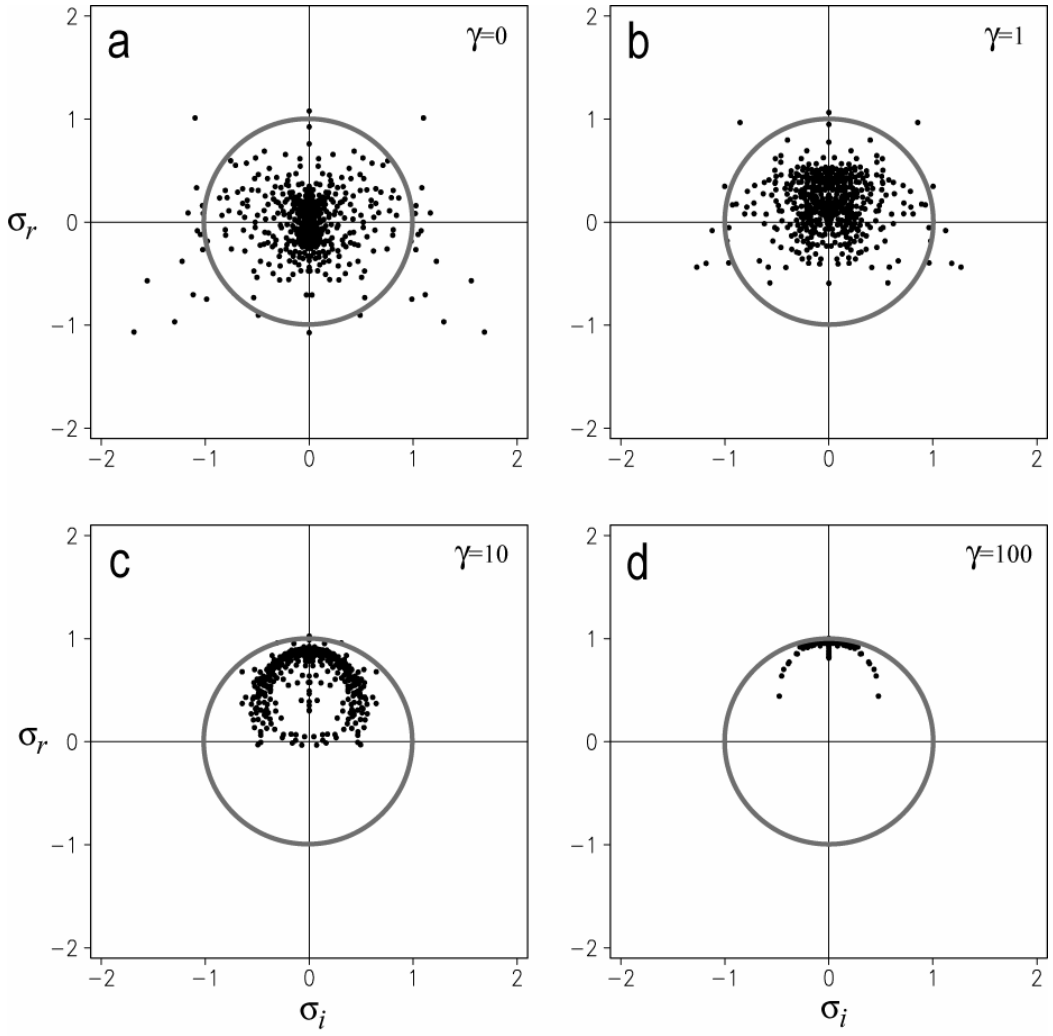

Fig.2 Eigenvalue spectrum of $\mathbf{M}^*$ in the T21 barotropic model with (a) $\gamma = 0$ (equal to $\mathbf{M}$), (b) $\gamma = 1$, (c) $\gamma = 10$, and (d) $\gamma = 100$. σ_i and σ_r are the imaginary and real parts, respectively. A unit circle is drawn for reference.

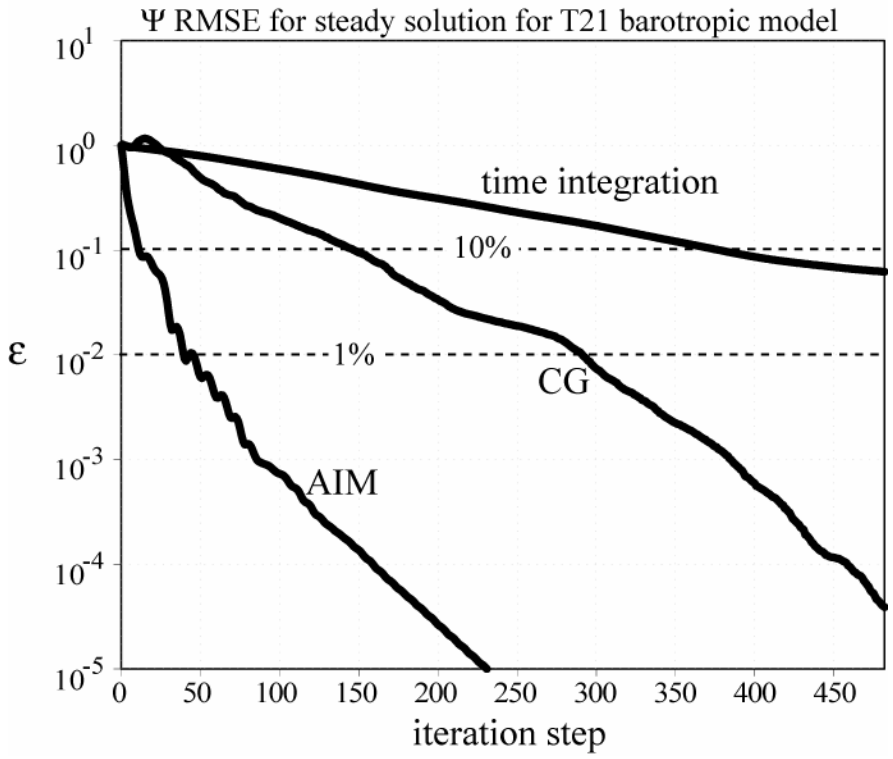

Fig.3 Same as Fig.1 but for ε calculated from three different methods: AIM with $\gamma = 7$, time integration, and conjugate gradient method. The 10% and 1% error levels are indicated by dashed lines. Note that three methods employ the same first guess.

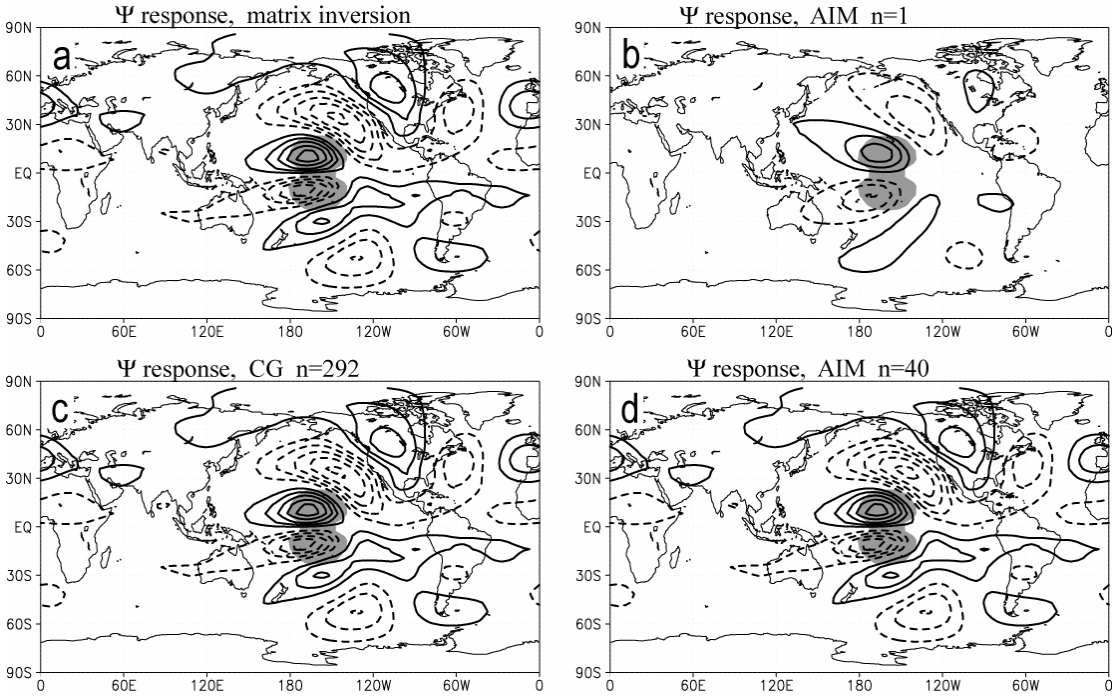

Fig.4 Steady streamfunction response to the equatorial divergent forcing (denoted by shading) obtained from the T21 barotropic model. The contour interval is 1×10^6 m^2 s^{-1} while the negative contours are dashed. (a) True solution by the matrix inversion, (b) the AIM solution at n=1 with $\gamma = 7$, (c) the CG solution at n=292, and (d) the AIM solution at n=40. The RMS errors for (c) and (d) are 1%.

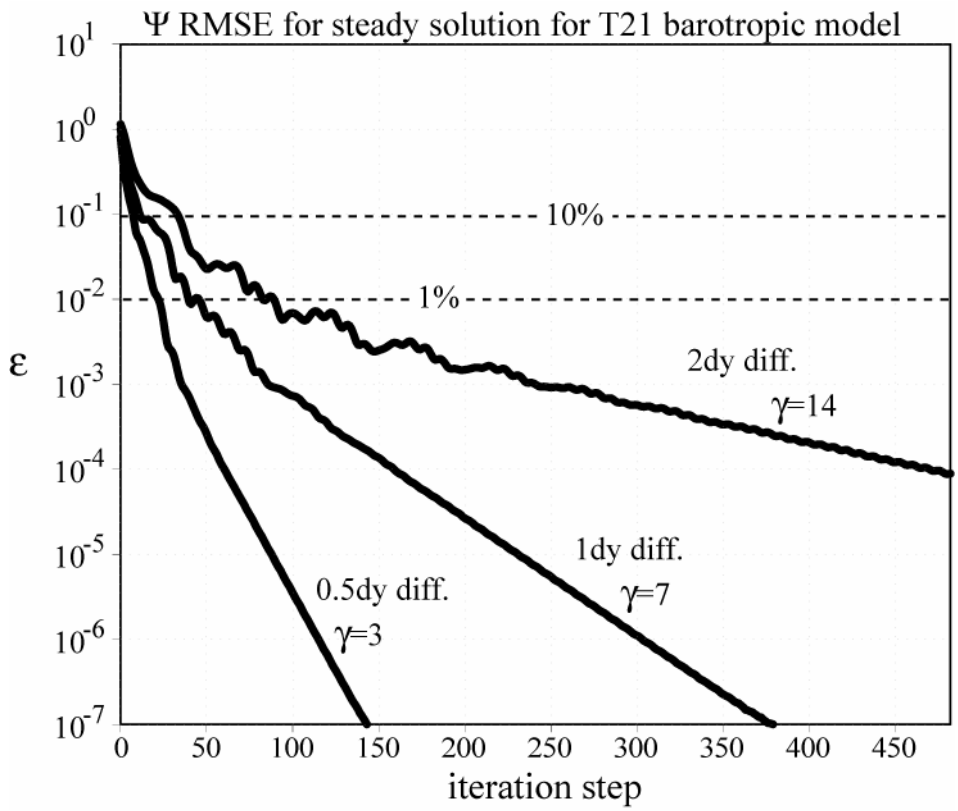

Fig.5 Same as Fig.1 but for ε calculated with different diffusion coefficients, varying from 12hr to 2dy damping timescale for the smallest wave. The best value of γ employed in each computation is also indicated.

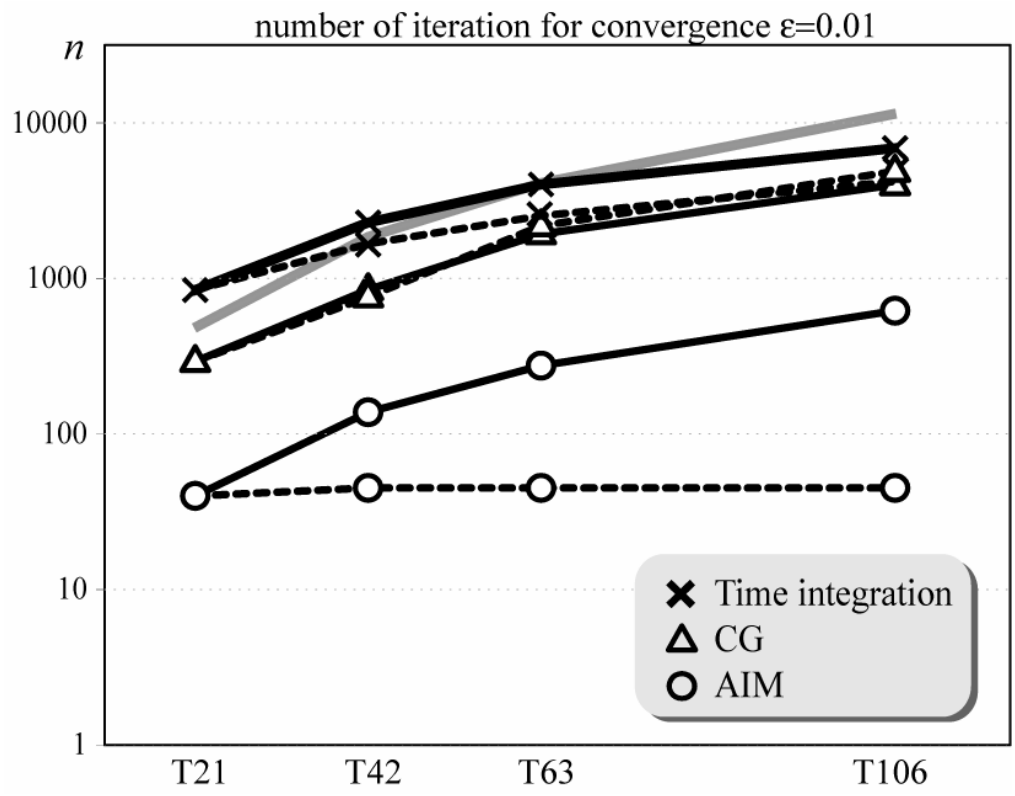

Fig.6 Number of iteration steps required for the convergence $\varepsilon \leq 0.01$ in the barotropic model with different horizontal resolution. Dashed lines with circle, triangle, and cross show the solutions obtained from AIM, CG, and time integration, respectively, all employing the diffusion coefficient common to the T21 resolution. Solid lines are the solutions with the diffusion dependent on the resolution (weaker in higher resolution, following Table 1). The gray line indicates the number of degrees of freedom.

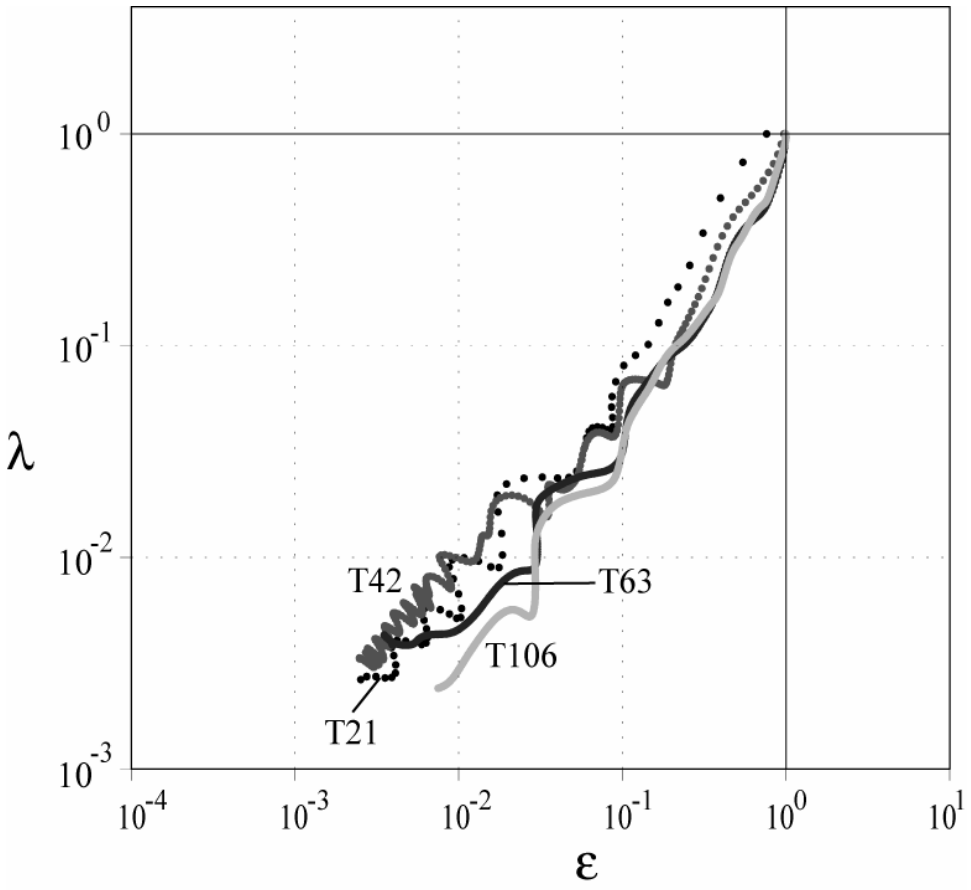

Fig.7 Differential norm ratio, λ, against the companion RMS error ratio, ε, for the AIM solutions in the barotropic model. The values are plotted up to n=70 for T21, n=300 for T42, n=400 for T63, and n=800 for T106, respectively. The diffusion timescale for each resolution follows Table 1.

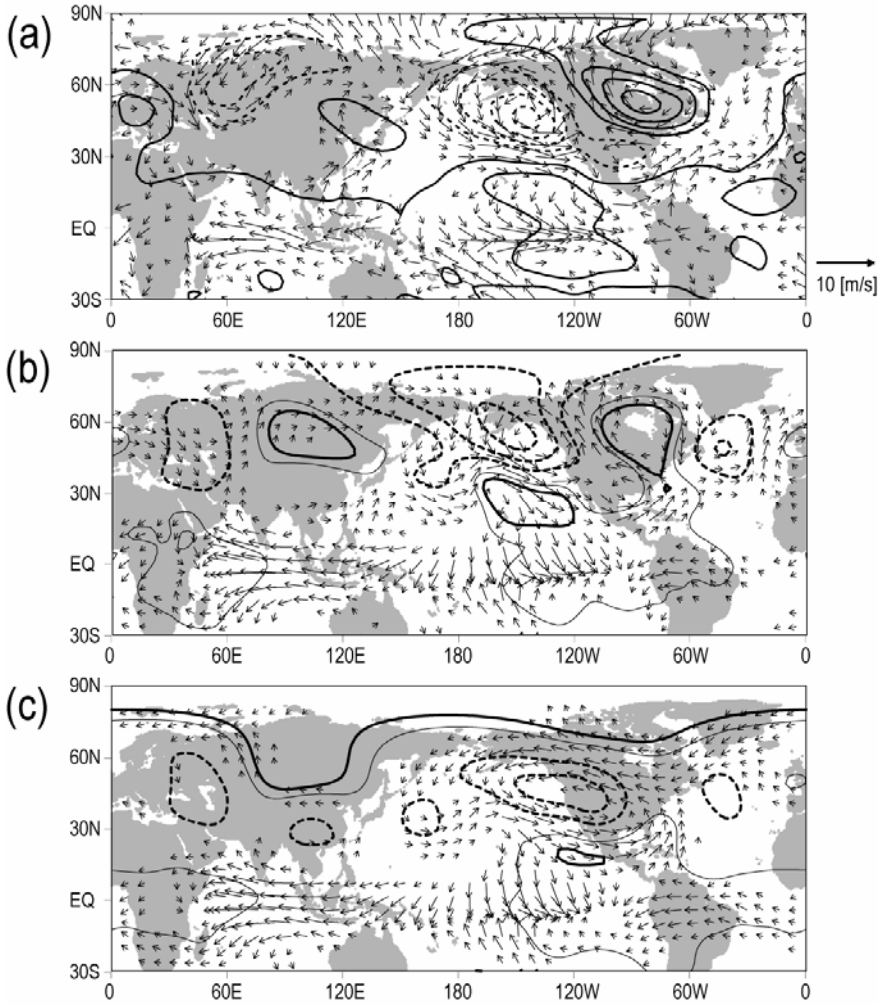

Fig.8 Anomalies of the 850 hPa wind (vector, plotted for the magnitude greater than 1 m s^{-1}) and 300 hPa geopotential height (contour, interval of 40 m without zero contours) (a) observed during winter 1997/98, and (b), (c) obtained as a steady response to the observationally estimated forcing. The responses are calculated with T42 20-level LBM, with the 3D basic state in (b) and the zonally uniform basic state in (c). The supplemental thin contour of 20 m is also indicated in (b) and (c).

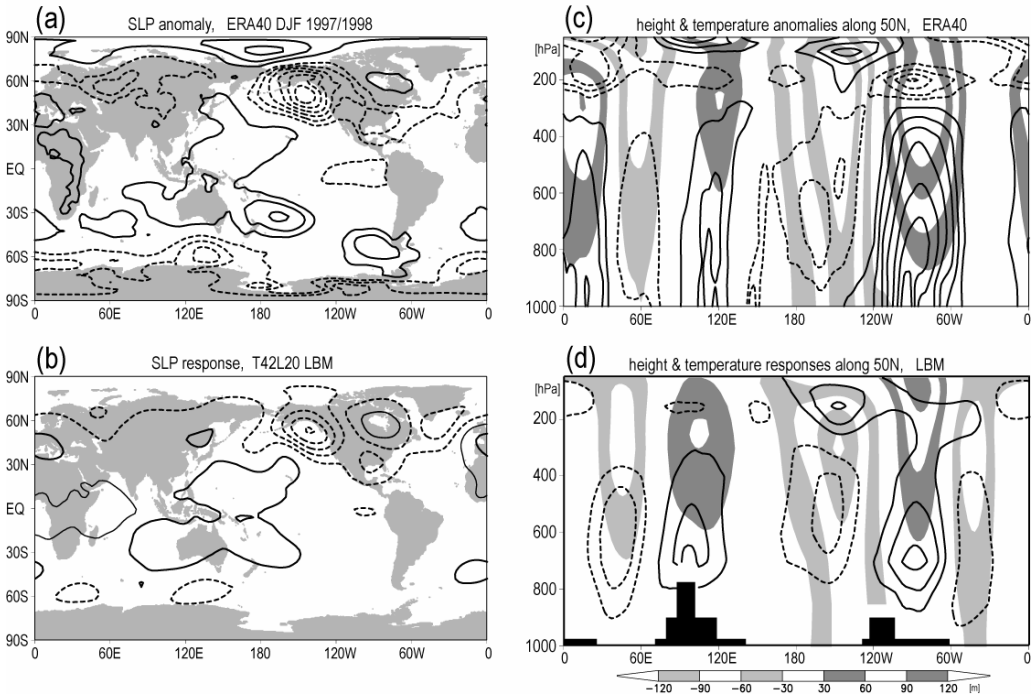

Fig.9 (a) Observed and (b) calculated SLP anomalies during winter 1997/98, the latter associated with the steady response shown in Fig. 8b. The contour interval is 2 hPa, the zero contours omitted. (c), (d) Same as (a), (b) but for the temperature (contour, 1K interval) and height (shading) anomalies along 50°N. Topography resolved in LBM is presented by the black rectangles in (d).

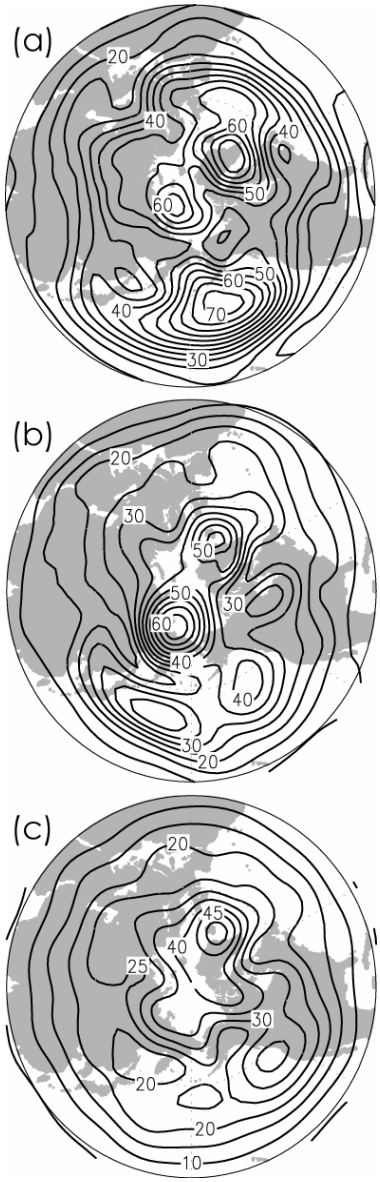

Fig.10 Standard deviations of the 500 hPa height anomalies during 1960-2002, obtained from (a) ERA40, (b) the T42 LBM hindcast, and (c) T42 SWM hindcast. The contour interval is 5m.

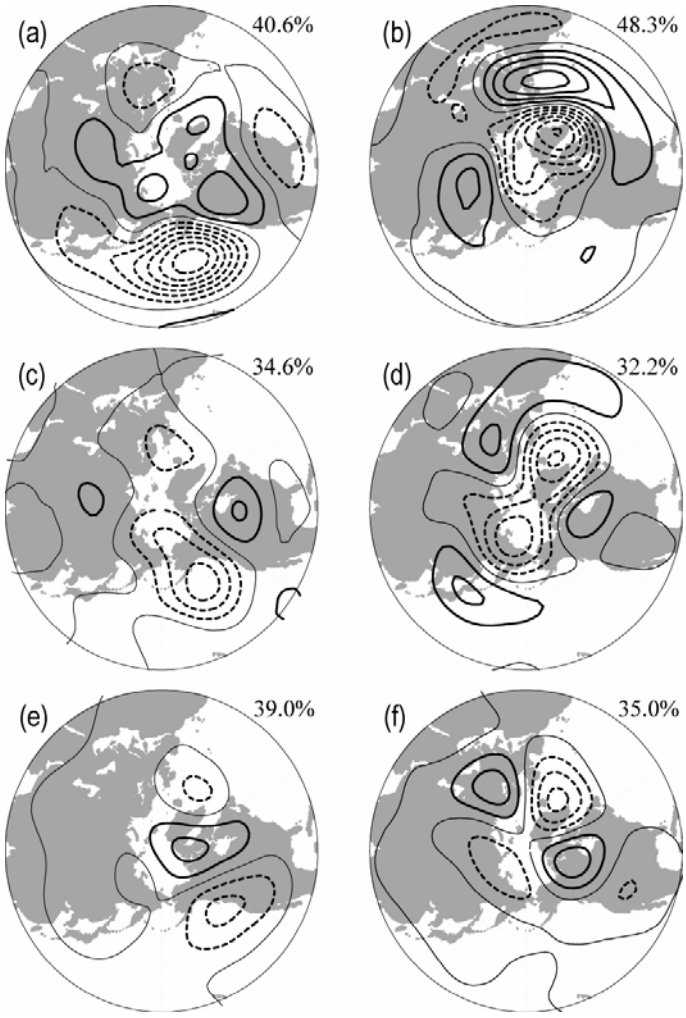

Fig.11 Leading EOFs to the winter SLP anomalies over the North Pacific (150°E-90°W, 20°-90°N) (left) and the North Atlantic (50°W-40°E, 20°-90°N) (right), as represented by the regression of the 500 hPa height anomalies on to the leading principal components in each sector. (a), (b) ERA40, (c), (d) LBM hindcast, and (e), (f) SWM hindcast. The contour interval is 10 m, with the zero line denoted by thin contour. The fractional variance of the respective EOF1 is also indicated at the top-right of each panel.

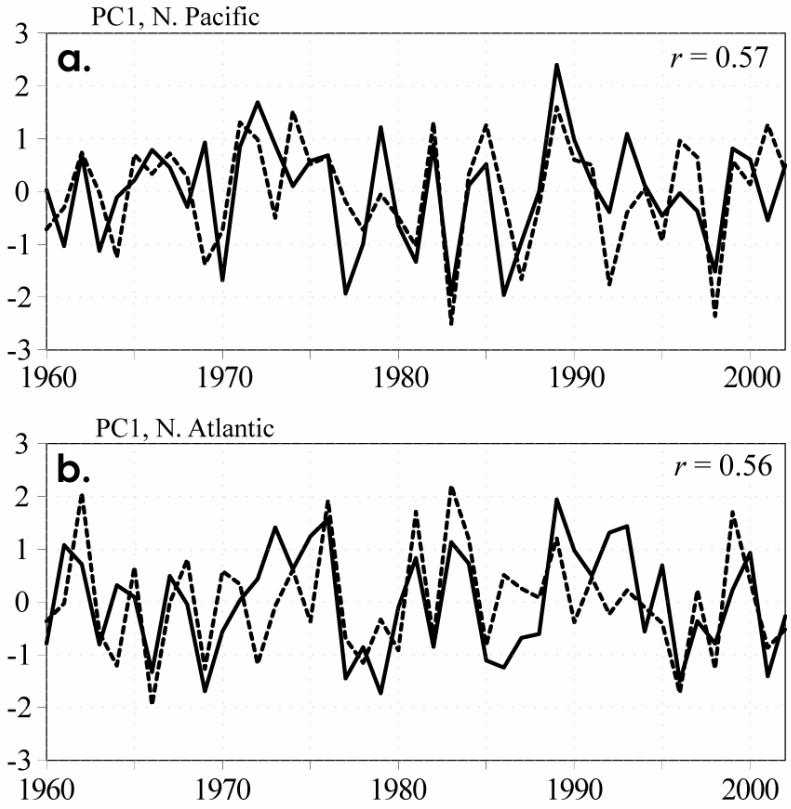

Fig.12 (a) The PC time series of the leading EOFs over the North Pacific shown in Fig. 11a, c. The solid (dashed) line indicates the observed (LBM hindcast) time series. (b) Same as (a) but for the leading EOFs over the North Atlantic shown in Fig. 11b, d. The correlation coefficients between the observed and hindcast time series are also shown at the top-right.

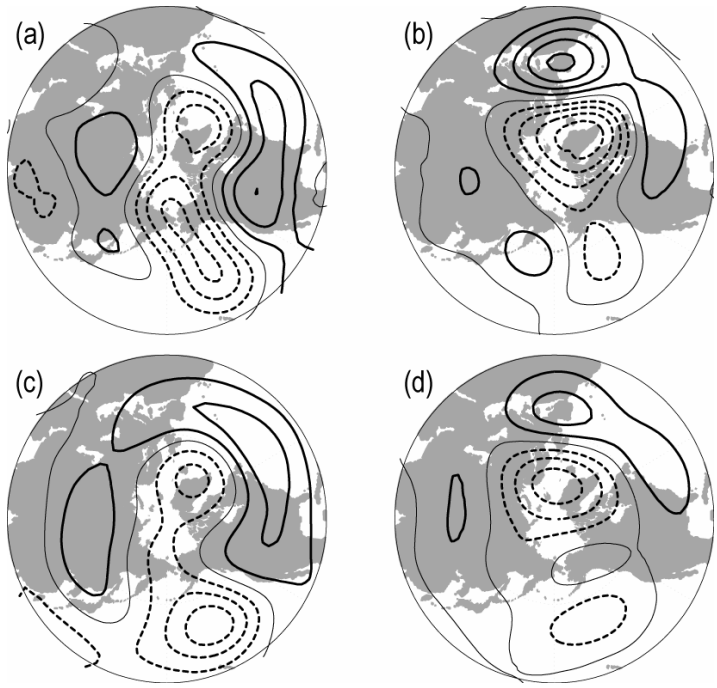

Fig.13 (a), (b) Same as Fig. 11c, d but for the regression of the hindcast response forced only by the diabatic heating anomalies. (c), (d) Same as (a), (b) but for the hindcast with zonally uniform basic state. The contour interval is 3 m.

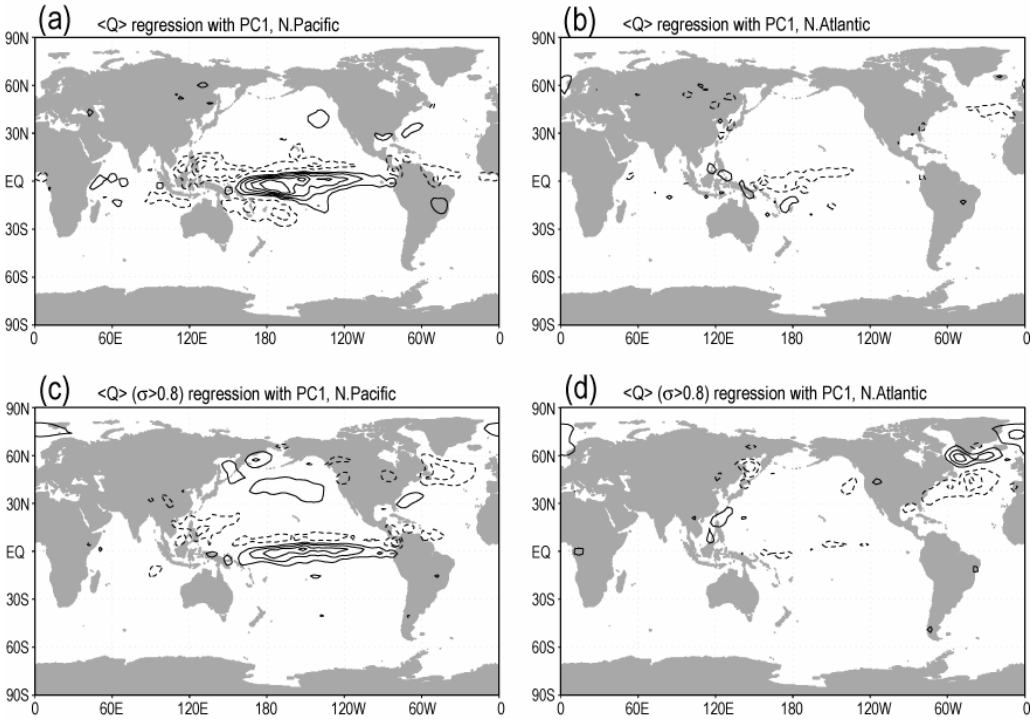

Fig.14 (a), (b) Same as Fig. 11c, d but for the regression of the vertically averaged heating. (c), (d) Same as (a), (b) but for the heating averaged in the lower troposphere ($\sigma \geq 0.8$). The contour interval is 0.2 K day^{-1}. The zero contours have been omitted and negative contours dashed.